The "Chain of Markers" code applied to large scale problems; solitary waves, sloshing and a plunging wave

Jørn Birknes-Berg[*][†]   Geir Pedersen[*]

1 Introduction

There are many different numerical methods for solving the Navier-Stokes equations for problems with a free surface. Some examples are volume of fluid (VOF), Marker and cell (MAC), level set, smooth particle hydrodynamics (SPH), boundary element methods (BEM) and weighted residual methods. One important element when solving problems with a free surface is how the free surface is treated. One of the most popular techniques is the VOF method. Another approach is to have markers on the free surface and this method is pursued in this study.

Correct implementation of the boundary conditions at the free surface is crucial when analyzing the wave propagation. For water waves the kinematic and dynamic bondary conditions need to be fulfilled, and the effect of imposing different boundary conditions at the free surface will be investigated in detail in the present study. The results will be compared with a boundary element method.

The Navier-Stokes solver applied in this report is the "Chain of Markers" code [9] and was originally used to study small scale problems like bubble collapse. Thus the code has a very accurate implementation of the surface tension (dynamic boundary condition). However, the present study is focusing on large scale problems and the "Chain of Markers" code has been reformulated in order to study plane (2D) waves. Both the Navier-Stokes and the BEM solver concidered here have only one phase, namely water. Air is not included in the models and is treated as void.

Results from the "Chain of Markers" code will be compared with a BEM solver. As discussed in section 2.3.3 it is important to numerically resolve the viscous boundary layer near the free surface when imposing the condition of surface tension. For small scale problems with small Reynolds numbers the boundary layer is thick while the opposite is the case for large scale problems. Thus imposing the surface tension condition for simulations where the boundary layer is poorly resolved may lead to inaccurate results, and a better approach is probably to disregard this effect.

---

[*]Mechanics Division, Department of Mathematics, University of Oslo, Norway
[†]DNV GL, Høvik, Norway

Both codes assumes an incompressible flow while the BEM solver also assumes irrotational flow. Two other options have been considered when studying the effect of the boundary conditions on the free surface with the "Chain of Markers"code. The first option is to impose a constraint for incompressible flow and the second is to impose a constraint for irrotational flow. The latter option is motivated by the BEM solver which is simulating incompressible and irrotational flow.

This study was carried out in 2004-2006 while Jørn Birknes-Berg was employed at the Department of Mathematics, University of Oslo as a Ph.D. student.

2 The Navier-Stokes equations

The incompressible Navier-Stokes equations is given by

$$\nabla \cdot \boldsymbol{v} = 0, \tag{1}$$

$$\frac{D\boldsymbol{v}}{dt} = -\frac{1}{\rho}\nabla p + 2\nu\nabla \cdot D + \boldsymbol{f}, \tag{2}$$

where ρ is the fluid density, ν is the kinematic viscosity, D is the strain rate tensor, $\boldsymbol{f}$ represents external forces and D/dt is the material derivate operator.

A finite volume formulation of the Navier-Stokes equations has been implemented in the "Chain of Markers" code and the description of the method is found in [9]. The code has been used to study small scale problems like bubble collapse, and for this reason it is assumed that the fluid flow is axisymmetric. In the present study, we will study two-dimensional problems and present the corresponding two-dimensional version of the numerical scheme.

Following the reference [9], the two-dimensional formulation of the Navier-Stokes equations may be written as

$$\frac{\partial u}{\partial x} + \frac{\partial w}{\partial z} = 0, \tag{3}$$

$$\frac{Du}{dt} = -\frac{\partial P}{\partial x} + \frac{\partial S_{xx}}{\partial x} + \frac{\partial S_{xz}}{\partial z}, \tag{4}$$

$$\frac{Dw}{dt} = -\frac{\partial P}{\partial z} + \frac{\partial S_{zz}}{\partial z} + \frac{\partial S_{zx}}{\partial x}, \tag{5}$$

where $P = p/\rho$ and the components of the stress tensor are

$$S_{xx} = 2\nu\frac{\partial u}{\partial x}, \quad S_{zz} = 2\nu\frac{\partial w}{\partial z}, \quad S_{xz} = S_{zx} = \nu\left(\frac{\partial w}{\partial x} + \frac{\partial u}{\partial z}\right). \tag{6}$$

The finite volume formulation of (3)–(5) is obtained by integrating the equations over an arbitrary domain Ω. If the velocity of the boundary of the domain $\partial\Omega$ is denoted by

$\hat{\boldsymbol{v}} = \hat{u}\boldsymbol{i} + \hat{w}\boldsymbol{k}$ it can be showed that

$$\int_{\partial\Omega} w \,\mathrm{d}x - \int_{\partial\Omega} u \,\mathrm{d}z = 0, \tag{7}$$

$$\frac{\partial}{\partial t} \int_{\Omega} u \,\mathrm{d}x\,\mathrm{d}z + \int_{\partial\Omega} u(w - \hat{w}) \,\mathrm{d}x - \int_{\partial\Omega} u(u - \hat{u}) \,\mathrm{d}z = \int_{\partial\Omega} P \,\mathrm{d}z$$
$$- \int_{\partial\Omega} S_{xx} \,\mathrm{d}z + \int_{\partial\Omega} S_{xz} \,\mathrm{d}x, \tag{8}$$

$$\frac{\partial}{\partial t} \int_{\Omega} w \,\mathrm{d}x\,\mathrm{d}z + \int_{\partial\Omega} w(w - \hat{w}) \,\mathrm{d}x - \int_{\partial\Omega} w(u - \hat{u}) \,\mathrm{d}z = - \int_{\partial\Omega} P \,\mathrm{d}x$$
$$+ \int_{\partial\Omega} S_{zz} \,\mathrm{d}x - \int_{\partial\Omega} S_{zx} \,\mathrm{d}z, \tag{9}$$

where we have applied Green's theorem and Reynolds transport theorem. The following sections 2.1 – 2.3 present the discrete volume formulation of the Navier-Stokes equations. We point out that these sections follow the reference [9] relatively closely, except that the equations presented here are valid for a 2D-Cartesian co-ordinate system, while the equations given in [9] are valid for axisymmetric problems.

2.1   The discrete formulation

When discretizing equations (7)–(9), we assume a staggered grid with equal spacing in both the horizontal and vertical direction, see figure 1. In the general case, the cell may be intersected by the free surface, which is illustrated in figure 1, and the contour integrals must be evaluated on the boundary $ABCDEA$. Referring to the figure, the velocity of the boundary of the cell equals zero on the horizontal and vertical edges while it equals the velocity of the free surface on CD.

Furthermore, it will be assumed that a quantity defined in the center of a cell, is constant over the whole cell, and quantities defined at the edges of a cell are constant over the edges. To simplify the notation, the following integral expressions for the cell (i, j) are introduced:

$$a^{i,j} = \int_{\Omega} \mathrm{d}x\,\mathrm{d}z,$$

$$S_z^{i,j-1/2} = \int_{AB} \mathrm{d}x, \qquad S_z^{i,j+1/2} = \int_{ED} \mathrm{d}x, \tag{10}$$

$$S_x^{i-1/2,j} = \int_{AE} \mathrm{d}z, \qquad S_x^{i+1/2,j} = \int_{BC} \mathrm{d}z.$$

The discrete finite volume formulation for the incompressibility condition (7) is then given by

$$(S_z w)^{i,j+1/2} - (S_z w)^{i,j-1/2} - (S_x u)^{i-1/2,j} + (S_x u)^{i+1/2,j} + \int_{\eta^{i,j}} w \,\mathrm{d}x - \int_{\eta^{i,j}} u \,\mathrm{d}z = 0. \tag{11}$$
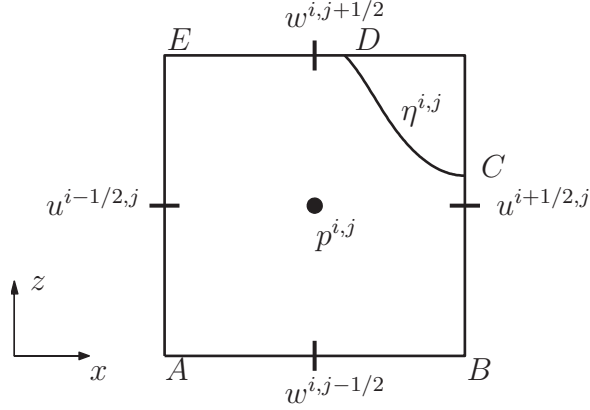
3

Figure 1: A sketch of the staggered grid where the free surface intersects the cell (i, j).

Similarly, the discrete version of the momentum equation (8)–(9) is given by

$$\frac{\partial}{\partial t}(au)^{i,j} + (S_z uw)^{i,j+1/2} - (S_z uw)^{i,j-1/2} - (S_x u^2)^{i-1/2,j} + (S_x u^2)^{i+1/2,j}$$

$$= (S_x P)^{i-1/2,j} - (S_x P)^{i+1/2,j} + \int_{\eta^{i,j}} P \, \mathrm{d}z$$

$$+ (S_z S_{xz})^{i,j+1/2} - (S_z S_{xz})^{i,j-1/2} + \int_{\eta^{i,j}} S_{xz} \, \mathrm{d}x$$

$$- (S_x S_{xx})^{i-1/2,j} + (S_x S_{xx})^{i+1/2,j} - \int_{\eta^{i,j}} S_{xx} \, \mathrm{d}z, \qquad (12)$$

$$\frac{\partial}{\partial t}(aw)^{i,j} + (S_z w^2)^{i,j+1/2} - (S_z w^2)^{i,j-1/2} - (S_x uw)^{i-1/2,j} + (S_x uw)^{i+1/2,j}$$

$$= -(S_z P)^{i,j+1/2} + (S_z P)^{i,j-1/2} - \int_{\eta^{i,j}} P \, \mathrm{d}x$$

$$+ (S_z S_{zz})^{i,j+1/2} - (S_z S_{zz})^{i,j-1/2} + \int_{\eta^{i,j}} S_{zz} \, \mathrm{d}x$$

$$- (S_x S_{zx})^{i-1/2,j} + (S_x S_{zx})^{i+1/2,j} - \int_{\eta^{i,j}} S_{zx} \, \mathrm{d}z. \qquad (13)$$

2.2   Operator splitting

The equations (7)–(9) will be solved by operator splitting, which is often referred to as pressure correction in the literature. In short, the method consists of two main steps. First, a predicted velocity is calculated by omitting the pressure gradient terms of the momentum equation. Thereafter, the pressure will be calculated to ensure a divergence free field, and the velocity is corrected. The equation for the pressure turns out to be a Poisson equation,

4

and this makes the method attractive since there exists a lot of solvers for this problem. To get an overview of different numerical methods for solving incompressible viscous flow, we refer to [6].

In the present study, the method of operator splitting will be applied to the finite volume representation of the Navier-Stokes equations. But for readability, the method is demonstrated for the Navier-Stokes equations (1) and (2).

Approximating the temporal derivative by a first order difference, the time discrete version of the Navier-Stokes equations that will be solved with this method is given by

$$\nabla \cdot \boldsymbol{v}^{n+1} = 0, \tag{14}$$

$$\frac{\boldsymbol{v}^{n+1} - \boldsymbol{v}^n}{\Delta t} + \boldsymbol{v}^n \cdot \nabla \boldsymbol{v}^n = -\frac{1}{\rho}\nabla p^{n+1} + 2\nu\nabla \cdot D^n + \boldsymbol{f}^n. \tag{15}$$

Neglecting the pressure gradient terms in (15), the predicted velocity $\boldsymbol{v}^*$ is given by the following explicit scheme:

$$\frac{\boldsymbol{v}^* - \boldsymbol{v}^n}{\Delta t} + \boldsymbol{v}^n \cdot \nabla \boldsymbol{v}^n = 2\nu\nabla \cdot D^n + \boldsymbol{f}^n. \tag{16}$$

The velocity at the new time is found by subtracting the equations (15) and (16). Hence,

$$\boldsymbol{v}^{n+1} = \boldsymbol{v}^* - \frac{\Delta t}{\rho}\nabla p^{n+1}, \tag{17}$$

and the equation for the pressure is found by requiring that $\nabla \cdot \boldsymbol{v}^{n+1} = 0$, leading to a Poisson equation for the pressure:

$$\nabla^2 p^{n+1} = \frac{\rho}{\Delta t}\nabla \cdot \boldsymbol{v}^*.$$

It is emphasized that the convective term in the Navier-Stokes equation is treated by upwind differences. A final comment to the method, is that the pressure needs some proper boundary conditions since the Poisson equation includes second-order derivatives of the pressure, while the original Navier-Stokes equations only have first order derivatives of the pressure. A discussion on this may be found in [6, 3].

Applying the the operator splitting method to the discrete formulation of the Navier-Stokes equations (11)–(13), we find that the expressions are not as short and elegant as described above. The prediction of the velocity is found by using a slightly modified version of equation (12) and (13) where the pressure gradient terms $(S_x P)^{i\pm1/2,j}$ and $(S_z P)^{i,j\pm1/2}$ are neglected, and the temporal derivative is approximated by a first order difference. After solving the equation for the pressure, the velocities are updated according to

$$
\begin{aligned}
u^{i,j} &= (u^*)^{i,j} + \frac{\Delta t}{a^{i,j}}\left((S_x P)^{i-1/2,j} - (S_x P)^{i+1/2,j}\right), \\
w^{i,j} &= (w^*)^{i,j} + \frac{\Delta t}{a^{i,j}}\left((S_z P)^{i,j-1/2} - (S_z P)^{i,j+1/2}\right),
\end{aligned}
\tag{18}
$$

which is the finite volume variant of equation (17). The velocities on the left hand side and the pressure, are evaluated at the new time $n+1$.

In order to establish the equation for the pressure, we assume that the velocity varies linearly from one side of the cell to the other. For cell (i,j) with sides equal to h, the velocities are expressed as

$$
\begin{aligned}
u(x)h &= (x - x^{i-1/2,j})u^{i+1/2,j} - (x - x^{i+1/2,j})u^{i-1/2,j}, \\
w(z)h &= (z - z^{i,j-1/2})w^{i,j+1/2} - (z - z^{i,j+1/2})w^{i,j-1/2}.
\end{aligned}
$$

Using these expressions, the integrals along the free surface are given by

$$
\begin{aligned}
\int_{\eta^{i,j}} w \, \mathrm{d}x &= \frac{w^{i,j+1/2}}{h} \int_{\eta^{i,j}} (z - z^{i,j-1/2}) \, \mathrm{d}x - \frac{w^{i,j-1/2}}{h} \int_{\eta^{i,j}} (z - z^{i,j+1/2}) \, \mathrm{d}x, \\
\int_{\eta^{i,j}} u \, \mathrm{d}z &= \frac{u^{i+1/2,j}}{h} \int_{\eta^{i,j}} (x - x^{i-1/2,j}) \, \mathrm{d}z - \frac{u^{i-1/2,j}}{h} \int_{\eta^{i,j}} (x - x^{i+1/2,j}) \, \mathrm{d}z.
\end{aligned} \tag{19}
$$

Finally, we can derive the equation for the pressure that will guarantee a divergence free velocity field. When using equation (18) and (19), we arrive at

$$
\begin{aligned}
&\frac{1}{\Delta t} \left[(S'_x u^*)^{i+1/2,j} - (S'_x u^*)^{i-1/2,j} + (S'_z w^*)^{i,j+1/2} - (S'_z w^*)^{i,j-1/2} \right] \\
&+ P^{i,j} \left\{ S_z^{i,j} \left(\left(\frac{S'_z}{a} \right)^{i,j+1/2} + \left(\frac{S'_z}{a} \right)^{i,j-1/2} \right) + S_x^{i,j} \left(\left(\frac{S'_x}{a} \right)^{i+1/2,j} + \left(\frac{S'_x}{a} \right)^{i-1/2,j} \right) \right\} \\
&\qquad\qquad = (S_z P)^{i,j+1} \left(\frac{S'_z}{a} \right)^{i,j+1/2} + (S_z P)^{i,j-1} \left(\frac{S'_z}{a} \right)^{i,j-1/2} \\
&\qquad\qquad + (S_x P)^{i+1,j} \left(\frac{S'_x}{a} \right)^{i+1/2,j} + (S_x P)^{i-1,j} \left(\frac{S'_x}{a} \right)^{i-1/2,j},
\end{aligned} \tag{20}
$$

where

$$
\begin{aligned}
(S'_x)^{i\pm1/2,j} &= (S_x)^{i\pm1/2,j} - \frac{1}{h} \int_{\eta^{i,j}} (x - x^{i\mp,j}) \, \mathrm{d}z, \\
(S'_z)^{i,j\pm1/2} &= (S_z)^{i,j\pm1/2} + \frac{1}{h} \int_{\eta^{i,j}} (z - z^{i,j\mp1/2}) \, \mathrm{d}x.
\end{aligned}
$$

Popinet and Zaleski [9] refer to (20) as a Poisson-like equation, and it is solved using multigrid-accelerated Gauss-Seidel relaxation, [1, 2, 10].

The numerical scheme applies adaptive time stepping, and the requirement to be fulfilled is that $C = \frac{\Delta t}{h} v_{max} \leq 0.5$, where C is the Courant number and v_{max} is the maximum horizontal or vertical velocity in the fluid field. If the Courant number is larger than 0.5, the time step will be reduced by a factor of two. On the other side, if $1.5C \leq 0.5$, the time step will be multiplied by 1.5.

2.3   Boundary conditions and extrapolation

An important aspect when solving the Navier-Stokes equations is the boundary conditions. Another issue is that the "Chain of Markers" code also need fluid velocities outside the free surface, and these velocities are obtained by extrapolating the fluid velocities near the free surface into the void. The boundary conditions and the extrapolation of the velocities are discussed in the following sections.

2.3.1   Free surface conditions

Several boundary conditions must be fulfilled on the free surface, and the dynamic boundary conditions are given by

$$p = p_0 + \sigma\kappa + \mu\boldsymbol{n} \cdot D \cdot \boldsymbol{n}, \tag{21}$$

$$\boldsymbol{t} \cdot D \cdot \boldsymbol{n} = 0. \tag{22}$$

In the expressions above p_0 is a constant isotropic pressure above the fluid, σ is the surface tension, κ is the curvature of the free surface, μ is the dynamic viscosity, and $\boldsymbol{n}$ and $\boldsymbol{t}$ are the normal and tangential vector of the free surface. These equations are also known as the stress balance equations. The former is used when evaluating the pressure on the free surface for equation (12) and (13), while the latter, expressing zero tangential stress on the free surface, may be used as a constraint when extrapolating the fluid velocity into the void, see section 2.3.3.

The kinematic boundary condition, stating that a fluid particle will remain on the free surface, is given by

$$\frac{D\boldsymbol{x}}{dt} = \boldsymbol{v}. \tag{23}$$

This equation is often written as $D\eta/dt = w$, but in order to allowing overturning waves, the version above is preferred. The free surface is defined as a cubic spline with a set of markers lying on the free surface in the "Chain of Markers" code, and at each time step the markers are moved according to a first order approximation of (23). It should also be noted that the velocity of the markers are extrapolated from the fluid velocities in the vicinity of the marker.

The "Chain of Markers" code was originally implemented for axisymmetric problems, and the dynamic and kinematic boundary conditions presented above, also apply for the axisymmetric case, except that the expressions for the curvature and the stress rate tensor differ for the 2D- and axisymmetric formulations.

2.3.2   Bottom and wall conditions

The boundary conditions on the bottom and fixed walls for the fluid velocity, are simply stated as $\boldsymbol{v} \cdot \boldsymbol{n} = 0$, where $\boldsymbol{n}$ is the normal vector of the boundary. In addition, an extra boundary condition is needed for the pressure when solving the Navier-Stokes equations

by the operator splitting method, and this is given by

$$\frac{\partial p}{\partial n} \equiv \boldsymbol{n} \cdot \nabla p = 0,$$

on the bottom and walls.

2.3.3 Extrapolation of the fluid velocities onto the free surface and into the void

Extrapolating the fluid velocities onto the free surface and into the void is an important aspect of this numerical implementation of the Navier-Stokes equations. This is due to the fixed grid and the need to move the markers on the free surface. Originally, the extrapolated velocities in the "Chain of Markers" code are solved by the method of Lagrange multipliers, and the markers on the free surface are moved under the constraint of zero tangential stress on the free surface.

Some assumptions need to be made when applying the method of Lagrange multipliers. In the vicinity of the point of interest, located near or on the free surface, it is assumed that the velocity field is linear $u(\boldsymbol{x}) = u_0 + A_{11}x + A_{12}y$ and $v(\boldsymbol{x}) = v_0 + A_{21}x + A_{22}y$, where $A_{i,j} = \frac{\partial u_i}{\partial x_j}$. The unknowns u_0, v_0 and A_{ij}, $i, j = 1, 2$ are then found by minimizing the function

$$\mathcal{F} = \sum_{i=1}^{N_x} (u_0 + A_{11}x_i + A_{12}y_i - u_i)^2 + \sum_{i=1}^{N_y} (v_0 + A_{21}x_i + A_{22}y_i - v_i)^2 + \sum_{i=1}^{N_\lambda} \lambda_i\, q_i, \quad (24)$$

where λ_i is a Lagrange multiplier, q_i is a constraint, and N_λ is the number of lagrange multipliers. N_x and N_y denote the number of points included in the horizontal and vertical direction due to the staggered grid, and these points are close to the point where the velocity is extrapolated. $\boldsymbol{u}_i = (u_i, v_i)$ is the velocity at position $\boldsymbol{x}_i = (x_i, y_i)$. Determining which points to be included in the sums above, requires a length measure. The simplest choice will be to just sum over the N_x and N_y closest points with respect to the Euclidean distance. However, a better alternative is to include information of the direction of the free surface normal vector $\boldsymbol{n}$ and also take into account whether the points are close to the line defined by the surface normal or close to the point where we want to extrapolate the velocity. Such a function might be expressed as

$$d(\boldsymbol{x}_i, \boldsymbol{x}_e) = A_n((\boldsymbol{x}_i - \boldsymbol{x}_e) \cdot \boldsymbol{n})^2 + A_t((\boldsymbol{x}_i - \boldsymbol{x}_e) \cdot \boldsymbol{t})^2,$$

where $\boldsymbol{t}$ is the tangential vector of the free surface, $\boldsymbol{x}_e$ is the point where we want to extrapolate the velocities, and A_n and A_t are coefficients with typically values of 1 and 2, respectively. A simple sketch is given in figure 2.

The "Chain of Markers" code has been developed for small scale problems like bubble collapse, and for these problems the Reynolds numbers are small. Physically, this means that there is a thick viscous boundary layer near the free surface, and it is possible to resolve the boundary layer properly for these numerical simulations. For simulations at
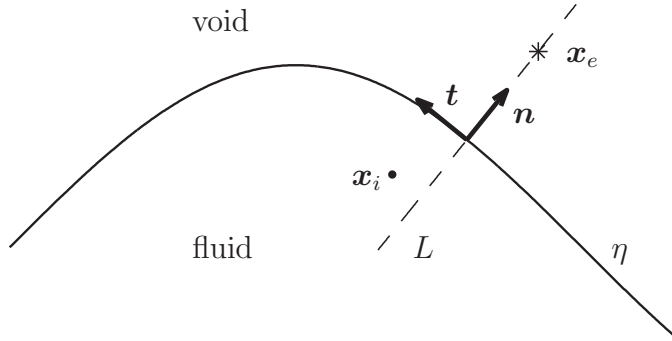
Figure 2: A sketch illustrating the extrapolation of velocities at $\boldsymbol{x}_e$ marked with an asterisk.

low Reynolds numbers, the boundary condition of zero tangential stress on the free surface is fulfilled by using the boundary condition (22) as a constraint in the method of Lagrange multipliers. Hence, one constraint is considered and $q_1 = \boldsymbol{t} \cdot D \cdot \boldsymbol{n}$.

On the other side, this study focuses on applications where the viscous boundary layer is thin. To illustrate the thickness of the boundary layer, Lamb has analyzed the effect of viscosity on water waves [5, Chap. XI, Art. 349], where it is assumed periodic waves, infinite water depth and linearized Navier-Stokes equations. The effect of the viscosity may be interpreted by looking at the non-dimensional vorticity in the field,

$$\omega \sim \exp(mz + ikx + nt), \tag{25}$$

where n is the complex wave frequency and m is the solution of the non-dimensional equation

$$(m^2 + k^2)^2 / Re^2 + k + We^{-1}k^3 = 4Re^{-2}k^3m, \tag{26}$$

where Re and We are the Reynolds and Weber numbers. A length and time scale, L and T, have been introduced to arrive at the non-dimensional expressions above, and the Reynolds and Weber number are defined by $Re = UL/\nu$ and $We = \rho U^2 L/\sigma$ where $U = L/T$ and σ is the surface tension. From (25) the magnitude of the vorticity is given by $|\omega| \sim \exp(\Re(m)z)$ when disregarding the time dependency. The real part of m is usually large for surface waves, and the effect of the viscosity decreases rapidly from the surface downwards. For this reason, the thickness of this viscous boundary layer may be defined as $\delta = 2\pi/\Re(m)$, and figure 3 shows the thickness for different Reynolds and Weber numbers.

From figure 3 it is seen that the thickness of the boundary layer is approximately 0.01 when the non-dimensional wave length is 20 ($Re = 10^6$ and $We = 10^4$). For comparison, some of the numerical simulations of solitary waves in this study have a wave length of 20, and the finest grid spacing which is possible with the "Chain of Markers" code, based on available computer power[1], is approximately 0.003 in both the horizontal and vertical direction. Hence, the width of the viscous boundary layer will only be modeled with three
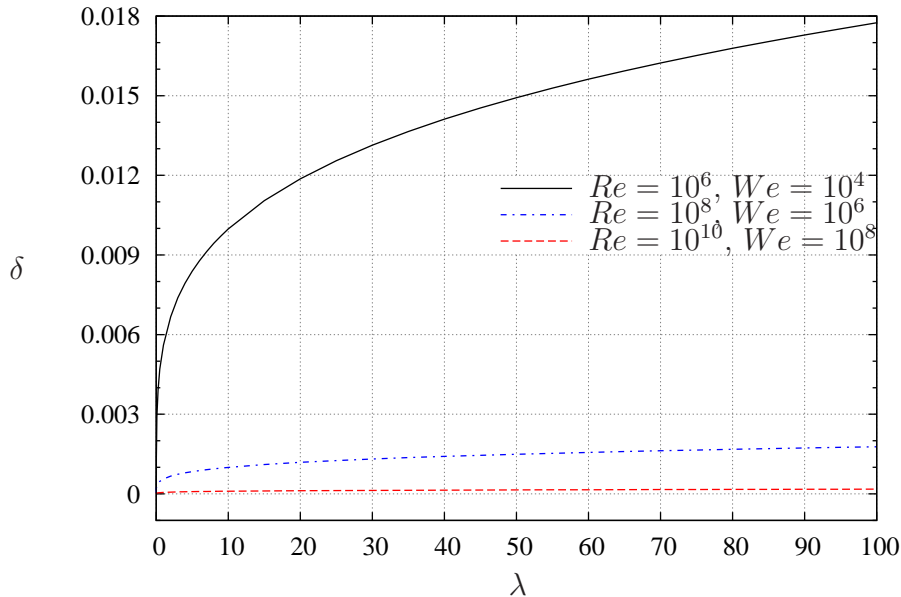
---

[1]The study was conducted in 2006.

Figure 3: Thickness δ of the viscous boundary layer for linear, periodic waves on infinite depth for different Reynolds and Weber numbers. δ and λ are non-dimensional.

grid points when the Reynolds number is of order 10^6. As seen from the figure, the thickness of the boundary layer decreases rapidly as the Reynolds number increases, which makes it practical impossible to resolve the boundary layer properly at high Reynolds number with the "Chain of Markers" code.

An important consequence of the analysis above, is that imposing zero tangential stress on the free surface will most likely lead to wrong results, and a better solution for simulations at high Reynolds number is to neglect that boundary condition. However, neglecting the Lagrange multiplier terms in equation (24) was not very successful when simulating solitary waves, because the simulations were aborted after only a few time steps, probably due to bad mass conservation. Instead, the condition of mass conservation was imposed when extrapolating the velocities. Furthermore, comparing results of the Navier-Stokes solver with other numerical codes simulating irrotational flow, motivates the constraint of zero curl. The importance of different constraints like $\nabla \cdot \boldsymbol{v} = 0$ and $\nabla \times \boldsymbol{v} = \boldsymbol{0}$, are demonstrated in section 3.

3   Simulations

In the following sections results for solitary waves, sloshing and plunging are presented. Inviscid flow is assumed, i.e. $Re = \infty$. Special attention is given to the effect of imposing different boundary conditions at the free surface. These will be incorporated as constraints when extrapolating the fluid velocity onto the free surface, refer to section 2.3.3 and equa-

tion (24). The different combinations consist of the following:

- Zero tangential stress on the free surface, $\boldsymbol{t} \cdot D \cdot \boldsymbol{n} = 0$.

- Incompressible flow, $\nabla \cdot \boldsymbol{v} = 0$.

- Incompressible and irrotational flow, $\nabla \cdot \boldsymbol{v} = 0$ and $\nabla \times \boldsymbol{v} = 0$.

In addition convergence tests and mass conservation properties have been investigated. Results are made non-dimensional and the length scale is equal to the mean water depth.

3.1 Norm

The L^2-norm has been applied to evaluate the difference between the BEM- and "Chain of Markers" solver, and the norm of the error is given by

$$||e||_{L^2(\Omega)} = \left(\int_\Omega e^2 \, \mathrm{d}\Omega \right)^{\frac{1}{2}}. \tag{27}$$

The error is defined by $e = u - \hat{u}$ where u is the reference solution and $\hat{u}$ is the solution that is compared with u.

3.2 Solitary wave

A solitary wave is a suitable problem for studying the effect of the different constraints on the free surface. In addition, several analytical properties are available for solitary waves that can be used for validating the results and evaluating the different constraints on the free surface. For more details about the solitary wave, we refer to references [4, 7, 11, 12].

The solitary wave considered has a relative large wave amplitude to water depth ratio, $a/h = 0.5$, and the horizontal length of the simulation domain is 60 times the water depth. For the finest discretization the horizontal length of the simulation domain is only $30h$ due to the long real-time simulation time. An overview of the grid resolutions are presented in table 1. Four different grids are used for the analysis, and the spacing between the nodes are reduced by a factor of two between the successive grids. The initial condition is generated by the boundary element method described in [8].

The mass conservation of each simulation is given in table 1, and from the table it is seen that the mass gain/loss is approximately reduced by a factor of two when the grid spacing is reduced accordingly. Another observation is that the boundary condition of zero tangential stress on the free surface yields the largest mass gain/loss in comparison with the two other boundary conditions.

Two properties of the solitary wave are that the wave is propagating with constant speed and shape. An approximation to the wave speed is given by $c_T = \sqrt{1 + a} + \mathcal{O}(a^2)$,

and the numerical wave speed c_0 and the initial position of the wave crest x_0 will be estimated by minimizing the function

$$\mathcal{H} = \sum_{i=1}^{N} (x_0 + c_0 t_i - x_p(t_i))^2 .$$

$x_p(t_i)$ defines the position of the maximum wave elevation at time t_i and N is the number of time steps. The correlation coefficient given by

$$r^2 = 1 - \frac{\sum_{i=1}^{N}(x_0 + c_0 t_i - x_p(t_i))^2}{\sum_{i=1}^{N}(x_p(t_i) - \bar{x}_p)^2},$$

is a measure of how well the model above describes the wave speed. $\bar{x}_p$ is the mean value of the wave crest, $\bar{x}_p = \sum_{i=1}^{N} x_p(t_i)/N$. Both the wave speed c_0 and the correlation coefficient r is given in table 2. As seen from the table, the numerical wave speed is approximately equal to the theoretical value for all the different grid resolutions, and the different choice of boundary condition is insignificant for this parameter. The correlation factor is also very close to 1 confirming that the numerical wave speed is constant. Using Tanaka's method to calculate the exact value of the wave speed it is found that $c_{T,exact} = 1.2158$ while the approximation above gives $c_T = 1.2247$. Hence, the normalized wave speed c_0/c_T in table 2 should be scaled by the factor $c_T/c_{T,exact} = 1.007$ for a more accurate comparison.

While the wave speed was more or less unaffected by the different grid resolutions and the choice of boundary condition on the free surface, this is not true for the wave amplitude. From figure 4 it is seen that the wave amplitude is decaying as the wave propagates, especially for the coarsest grids. For the case with zero tangential stress on the free surface and the coarsest grid, see figure 4(a), the wave amplitude is reduced by 11% after the wave has propagated a distance of 45 depths ($t = 37$). But as the grids get denser, the amplitude decay diminishes, and for these analyses the best results with respect to the amplitude decay are achieved for the cases with the incompressible fluid constraints on the free surface, see figure 4(b) and 4(c).

Table 1: Mass conservation $\max(|M(t)-M(0)|/M_R)$ for different boundary conditions (BC) and grids. M_R is a reference mass and equals the mass above the still water line for $t = 0$. A negative value means loss of mass.

BC / Grid		$\boldsymbol{t}\cdot D\cdot\boldsymbol{n}=0$	$\nabla\cdot\boldsymbol{v}=0$	$\nabla\cdot\boldsymbol{v}=0,$ $\nabla\times\boldsymbol{v}=0$
Grid size	Δx			
512×16	1.20E-01	5.81E-02	4.22E-02	2.45E-02
1024×32	5.81E-02	2.72E-02	2.10E-02	7.91E-03
2048×64	2.86E-02	1.87E-02	1.21E-02	9.34E-03
2048×128	1.42E-02	2.17E-03	2.00E-03	1.27E-03

Table 2: Wave speed c_0/c_T and the correlation coefficient r for different boundary conditions (BC) and grids.

BC / Grid		$\boldsymbol{t}\cdot D\cdot\boldsymbol{n}=0$		$\nabla\cdot\boldsymbol{v}=0$		$\nabla\cdot\boldsymbol{v}=0,$ $\nabla\times\boldsymbol{v}=0$	
Grid size	Δx	c_0/c_T	r	c_0/c_T	r	c_0/c_T	r
512×16	1.20E-01	0.99354	0.999992	0.99709	0.999995	0.99236	0.999994
1024×32	5.81E-02	0.99329	0.999998	0.99557	0.999999	0.99215	0.999998
2048×64	2.86E-02	0.99244	0.999999	0.99466	1.000000	0.99196	1.000000
2048×128	1.42E-02	0.99430	0.999999	0.99583	0.999999	0.99359	0.999999

(a) $\boldsymbol{t} \cdot D \cdot \boldsymbol{n} = 0$

(b) $\nabla \cdot \boldsymbol{v} = 0$

(c) $\nabla \cdot \boldsymbol{v} = 0$ and $\nabla \times \boldsymbol{v} = 0$
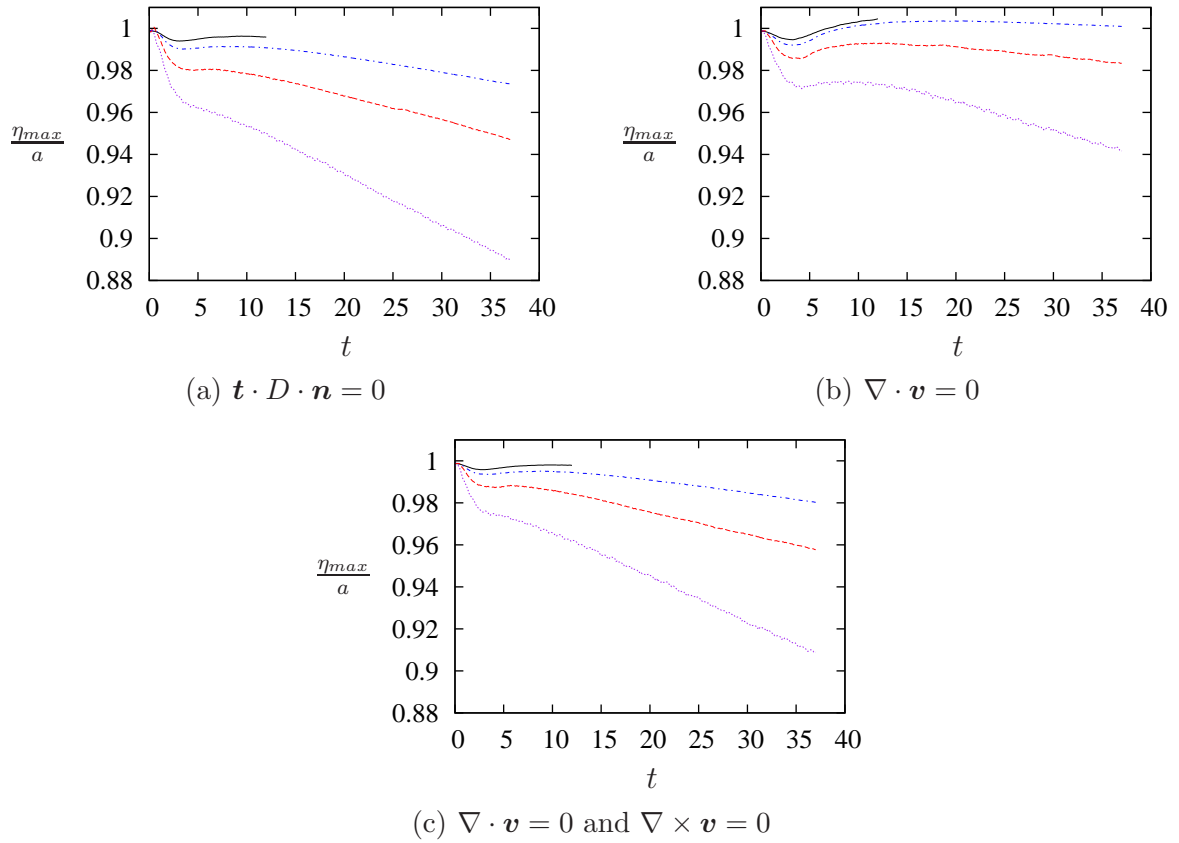
Figure 4: Maximum wave elevation normalized by the amplitude for different boundary conditions. Solid line: 2048×128 points; dash-dot line: 2048×64 points; dashed line: 1024×32 points; dotted line: 512×16 points.

14

3.3 Sloshing

A different problem than the solitary wave presented in section 3.2 is sloshing in a tank. While the solitary wave is propagating with constant shape and speed, sloshing is a more untidy motion. For realistic sloshing problems there will be wave breaking, large slamming forces on the walls and air-water mixturing. However, covering the general sloshing problem is beyond the scope of this study, and a simplified sloshing problem will be analyzed assuming a non-moving tank with fixed walls. The bottom of the tank is horizontal and located at $z = -h = -1$ and the vertical side walls are positioned at $x = 0$ and $x = L_T$. Initially, the fluid velocity is zero and the surface elevation is given by

$$\eta_0 = \begin{cases} \frac{1}{2}a\left(1 + \cos(\pi\frac{x}{L})\right), & 0 \leq x \leq L, \\ 0, & L < x \leq L_T. \end{cases}$$

For these simulations the parameters a, L and L_T are defined by $a/h = 0.5$, $L = 1.0$ and $L_T = 2L$. The initial surface elevation is seen in figure 5 together with a convergence test for the reference solution (BEM) and is described in [8].

A convergence test of the reference solution is shown in figure 5 where the results of four different grids are presented. The spatial resolution is systematically refined, and the coarsest grid has a spatial resolution $\Delta x = 0.105$, while the finest grid has $\Delta x = 0.0126$. Some snapshots of the wave elevation are shown in the figure, and the solution converges nicely. In the case of the finest mesh, the wave breaks for $t \approx 2.3$ and the numerical solution breaks down. For this reason the comparison between the BEM- and the "Chain of Markers" method is performed for times less than $t = 2.3$.

Three different surface constraints (zero tangential stress on the free surface, incompressible fluid, and incompressible and irrotational fluid) and four different grid resolutions are considered. Table 5 shows the the mass conservation for the different grids and surface constraints, and for all the cases reported in the table the relative mass conservation is of order 10^{-3}. It is also noted that the mass loss/gain decreases as the grid resolution increases except for the finest grids for two of the surface constraints. In addition, it is seen that the zero tangential stress condition on the free surfaces results in the highest mass loss/gain compared to the two other free surface constraints. Table 4 is summarizing the error for the different grid resolutions, and it is observed that the smallest error is achieved for the case with both incompressible and irrotational flow. A more visual comparison of the grid dependency ispresented in figure 6 where results based on a coarse and fine grid are shown. It is noticed that the results is more affected by the combination of boundary constraints than the grid resolution.

Convergence tests for the different boundary constraints are presented in figure 7 to 9. Common for all cases is that the Navier-Stokes solution is converging to the BEM solution. As expected the case with the surface tension included is converging slower than the two other. A comparison between the BEM and the Navier-Stokes solver is presented in figure 10-13. Especially for the fine grid good agreement is achieved. But it is also interesting to see that the results based on the coarse grid gives a good approximation to the BEM solution.

Finally, the relative errors between the maximum value of the free surface of the two solvers are compared, and the results are presented in figure 14 and 15. As confirmed by the other results presented in this section, it is seen that the difference between the maximum wave elevation is largest for the case with surface tension included.

Table 3: Convergence test for the BEM method at $t = 2.0$.

Grid no.	Δx	Error norm
2	1.05E-01	3.68E-04
4	5.13E-02	6.15E-05
8	2.53E-02	6.66E-06
16	1.26E-02	4.03E-07

Table 4: Convergence test for the different boundary conditions (BC) at $t = 2.0$.

		Error norm		
Grid	BC	$\boldsymbol{t} \cdot D \cdot \boldsymbol{n} = 0$	$\nabla \cdot \boldsymbol{v} = 0$	$\nabla \cdot \boldsymbol{v} = 0$, $\nabla \times \boldsymbol{v} = \boldsymbol{0}$
Grid size	Δx			
64×64	3.13E-02	1.10E-03	6.08E-04	3.38E-04
128×128	1.56E-02	6.05E-04	3.47E-04	1.66E-04
256×256	7.81E-03	3.35E-04	1.73E-04	5.56E-05
512×512	3.91E-03	1.86E-04	9.80E-05	2.58E-05

Table 5: Mass conservation $\max(|M(t) - M(0)|/M_R)$ for different boundary conditions (BC), grids and $t = 2.3$. M_R is a reference mass and equals the mass above $z = 0$ for $t = 0$. A negative value means loss of mass.

Grid		Mass conservation		
BC		$\boldsymbol{t} \cdot D \cdot \boldsymbol{n} = 0$	$\nabla \cdot \boldsymbol{v} = 0$	$\nabla \cdot \boldsymbol{v} = 0,$ $\nabla \times \boldsymbol{v} = \boldsymbol{0}$
Grid size	Δx			
64×64	3.13E-02	-8.32E-03	-2.93E-03	-1.98E-03
128×128	1.56E-02	-4.18E-03	-2.00E-03	-1.60E-03
256×256	7.81E-03	-2.16E-03	-1.12E-03	-1.28E-03
512×512	3.91E-03	-1.79E-03	-1.46E-03	-1.57E-03
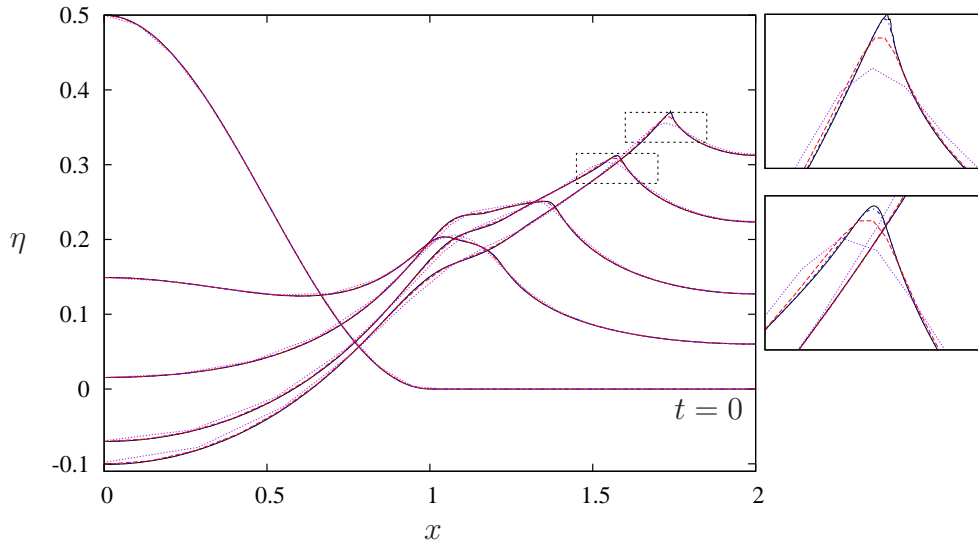
Figure 5: Convergence test for the reference solution (BEM), $t = \{0, 1.2, 1.6, 2, 2.3\}$. Solid line: $\Delta x = 0.0126$; dash-dot line: $\Delta x = 0.0253$; dashed line: $\Delta x = 0.0513$; dotted line: $\Delta x = 0.105$.
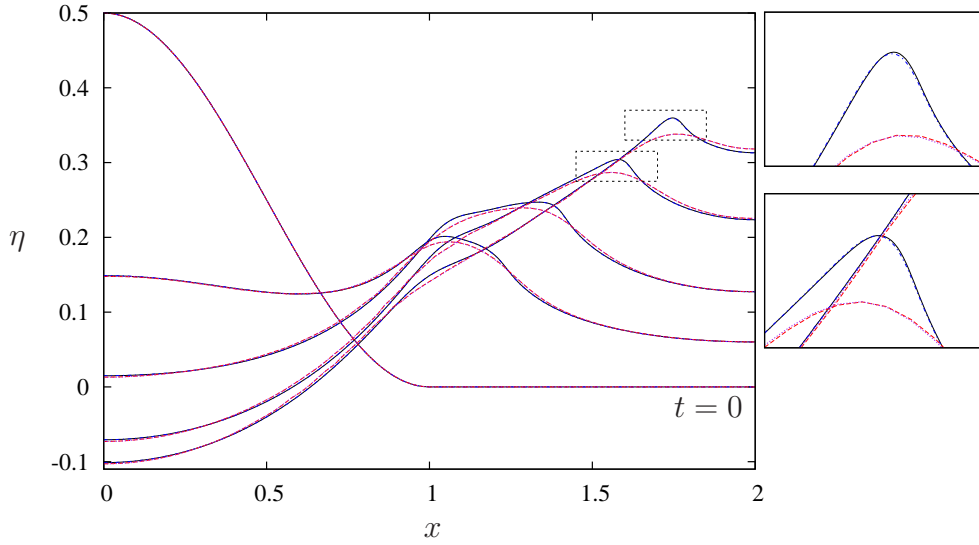
Figure 6: The wave elevation for different boundary conditions on the free surface for a dense and coarse grid, $t = \{0, 1.2, 1.6, 2, 2.3\}$. Solid line: $\boldsymbol{t} \cdot D \cdot \boldsymbol{n} = 0$; dash-dot line: $\boldsymbol{t} \cdot D \cdot \boldsymbol{n} = 0$ and $\nabla \cdot \boldsymbol{v} = 0$; dashed: $\boldsymbol{t} \cdot D \cdot \boldsymbol{n} = 0$; dotted line: $\boldsymbol{t} \cdot D \cdot \boldsymbol{n} = 0$ and $\nabla \cdot \boldsymbol{v} = 0$. The two former curves are based on a grid of 512×512 points, while the two latter are based on a grid of 64×64 points. (The lines for each grid more or less coincide for each grid resolution.)
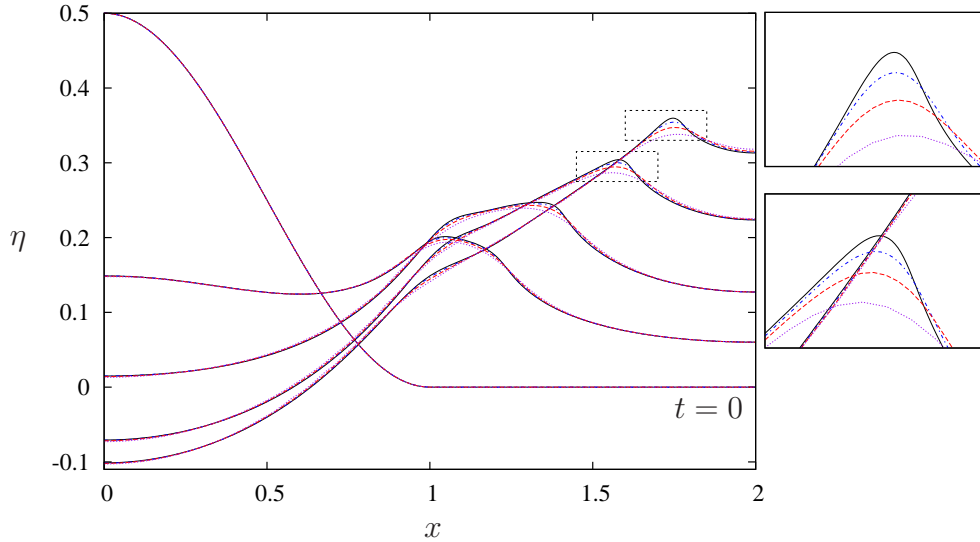
Figure 7: Convergence test when $\boldsymbol{t} \cdot D \cdot \boldsymbol{n} = 0$ is applied for the extrapolation near the free surface, $t = \{0, 1.2, 1.6, 2, 2.3\}$. Solid line: 512×512 points; dash-dot line: 256×256 points; dashed line: 128×128 points; dotted line: 64×64 points.

18
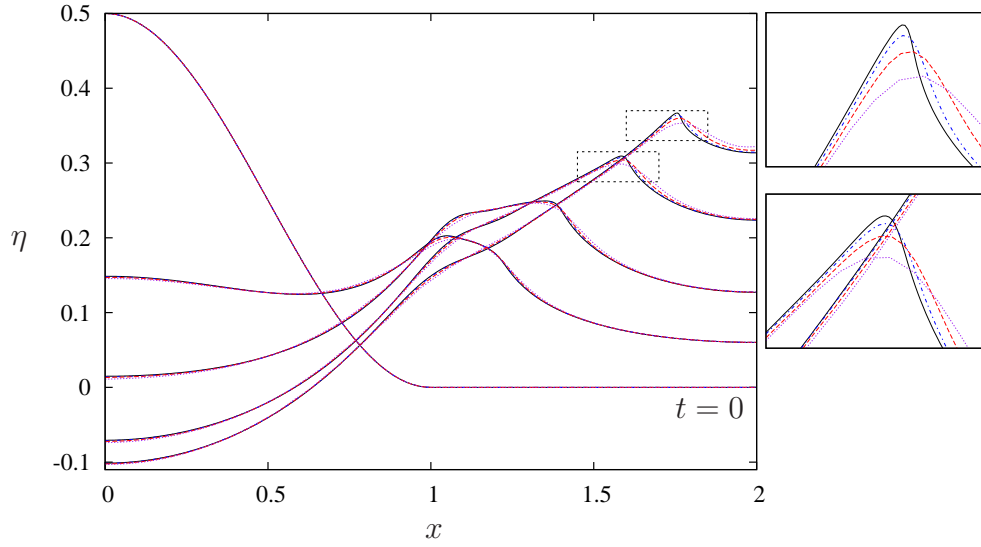
Figure 8: Convergence test when $\nabla \cdot \boldsymbol{v} = 0$ is applied for the extrapolation near the free surface, $t = \{0, 1.2, 1.6, 2, 2.3\}$. Solid line: 512×512 points; dash-dot line: 256×256 points; dashed line: 128×128 points; dotted line: 64×64 points.
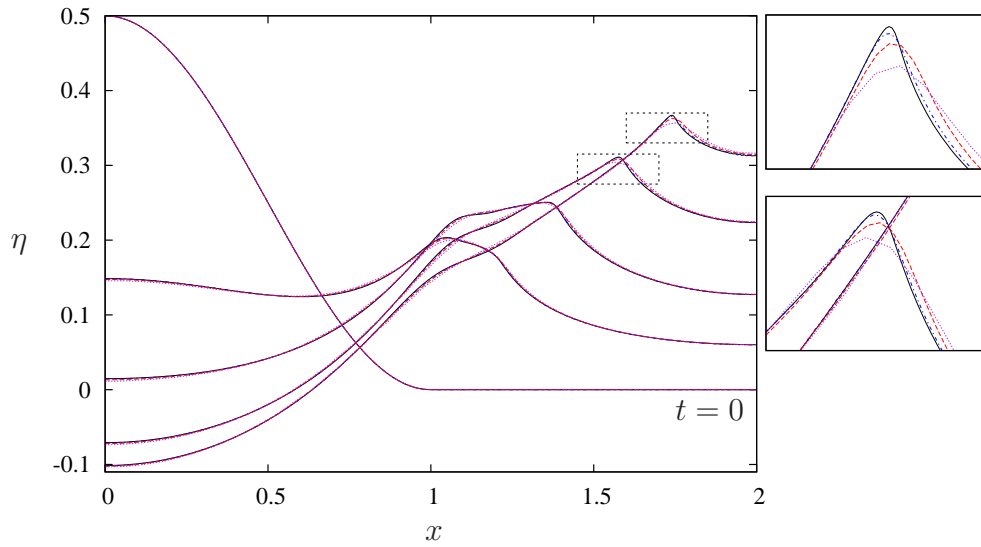
Figure 9: Convergence test when $\nabla \cdot \boldsymbol{v} = 0$ and $\nabla \times \boldsymbol{v} = 0$ is applied for the extrapolation near the free surface, $t = \{0, 1.2, 1.6, 2, 2.3\}$. Solid line: 512×512 points; dash-dot line: 256×256 points; dashed line: 128×128 points; dotted line: 64×64 points.
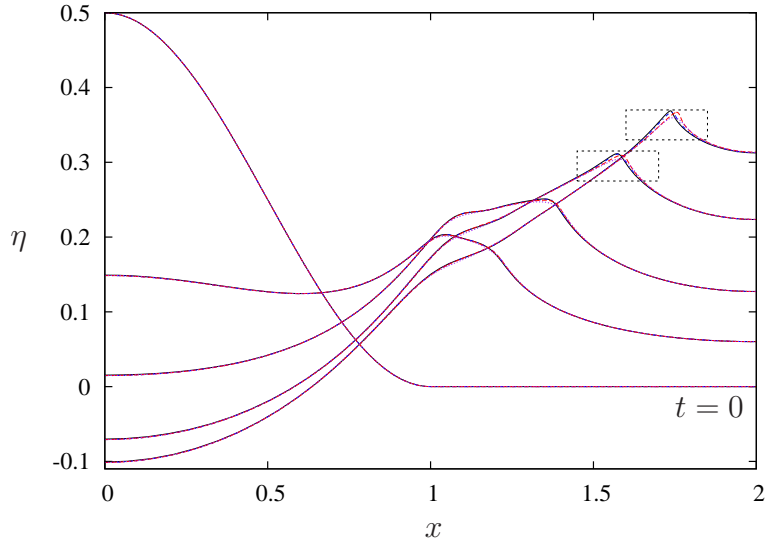
Figure 10: The wave elevation for different boundary conditions on the free surface, $t = \{0, 1.2, 1.6, 2, 2.3\}$ compared against the BEM results. The grid for the "Chain of Markers" code is 512×512 points. Solid line: BEM; dash-dot line: $\nabla \cdot \boldsymbol{v} = 0$ and $\nabla \times \boldsymbol{v} = 0$; dashed line: $\nabla \cdot \boldsymbol{v} = 0$; dotted line: $\boldsymbol{t} \cdot D \cdot \boldsymbol{n} = 0$. Close-ups, as indicated by the two boxes, are shown in figure 12.
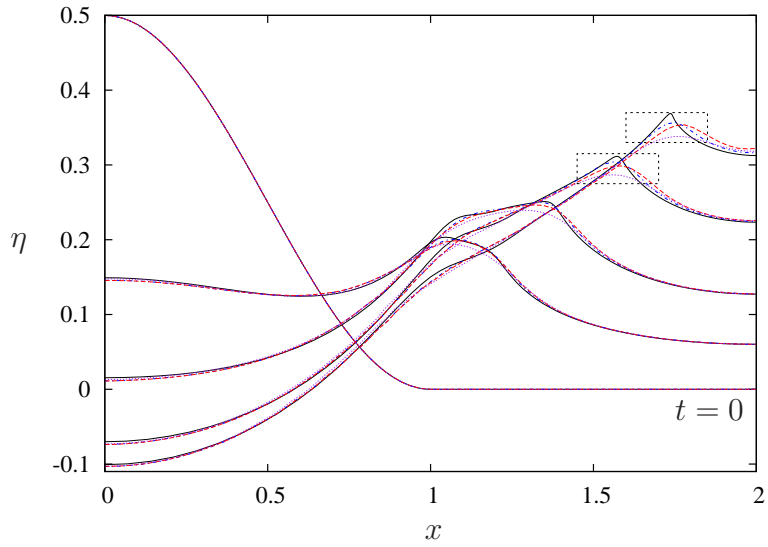
Figure 11: The wave elevation for different boundary conditions on the free surface, $t = \{0, 1.2, 1.6, 2, 2.3\}$ compared against the BEM results. The grid for the "Chain of Markers" code is 66×66 points. Solid line: BEM; dash-dot line: $\nabla \cdot \boldsymbol{v} = 0$ and $\nabla \times \boldsymbol{v} = 0$; dashed line: $\nabla \cdot \boldsymbol{v} = 0$; dotted line: $\boldsymbol{t} \cdot D \cdot \boldsymbol{n} = 0$. Close-ups, as indicated by the two boxes, are shown in figure 13.

20
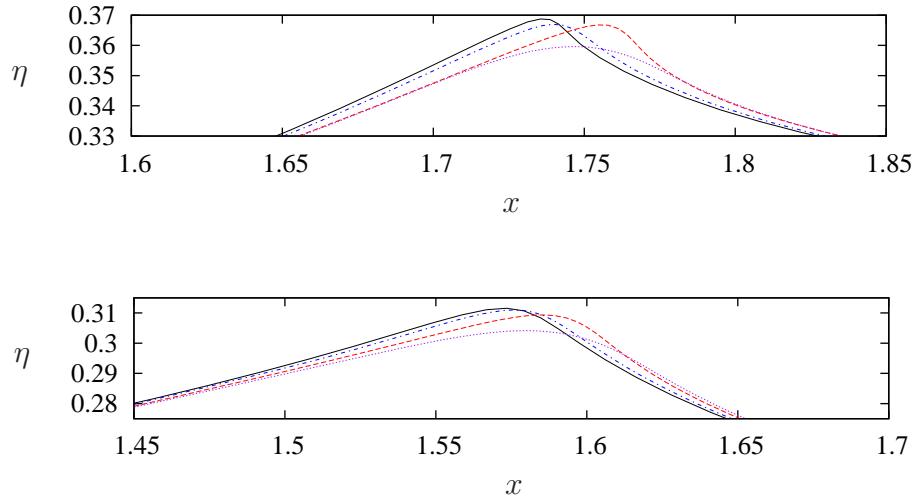
Figure 12: Close-ups of the wave elevation as indicated by the boxes in figure 10. Upper: $t = 2.3$; lower: $t = 2$. Grid for the "Chain of Markers": 512×512.
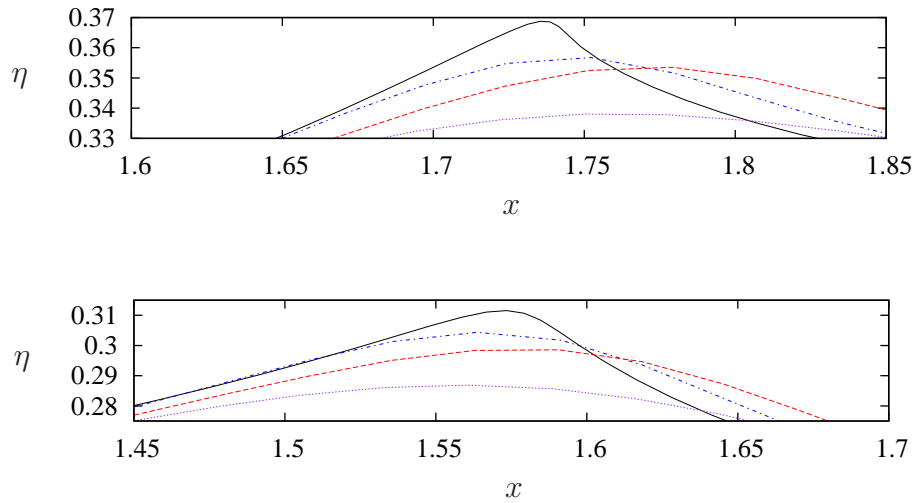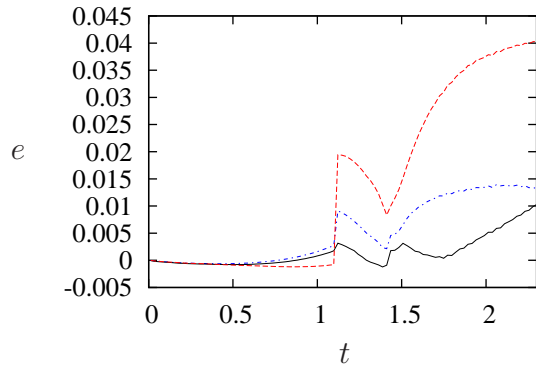

Figure 13: Close-ups of the wave elevation as indicated by the boxes in figure 11. Upper: $t = 2.3$; lower: $t = 2$. Grid for the "Chain of Markers": 66×66.
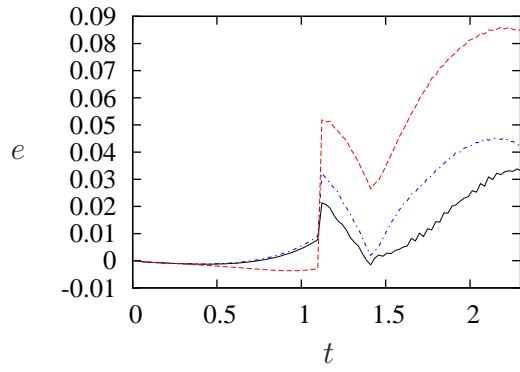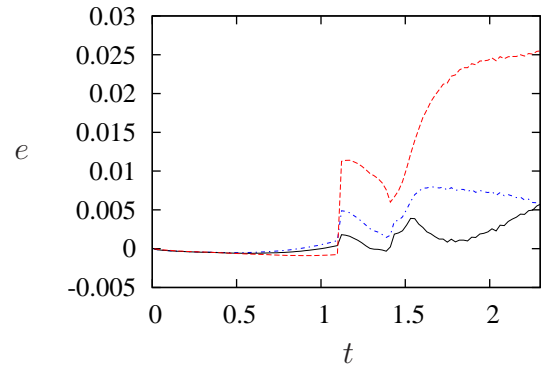
(a) 64 × 64 points
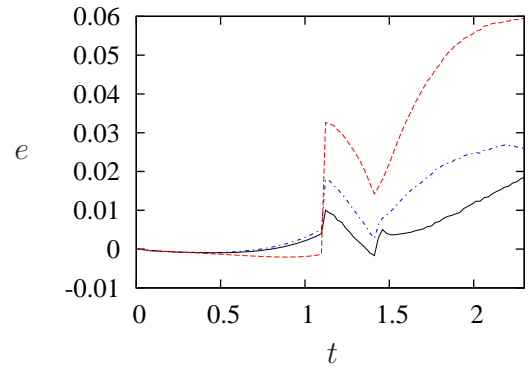
(b) 128 × 128 points

(c) 256 × 256 points

(d) 512 × 512 points

Figure 14: Relative error, $e = [\max(\eta_{BEM}) - \max(\eta_{NS})]/\max(\eta_{BEM})$, for different grids. Solid line: $\nabla \cdot \boldsymbol{v} = 0$ and $\nabla \times \boldsymbol{v} = 0$; dash-dot line: $\nabla \cdot \boldsymbol{v} = 0$; dashed line: $\boldsymbol{t} \cdot D \cdot \boldsymbol{n} = 0$.

(a) $\boldsymbol{t} \cdot D \cdot \boldsymbol{n} = 0$

(b) $\nabla \cdot \boldsymbol{v} = 0$

(c) $\nabla \cdot \boldsymbol{v} = 0$ and $\nabla \times \boldsymbol{v} = 0$
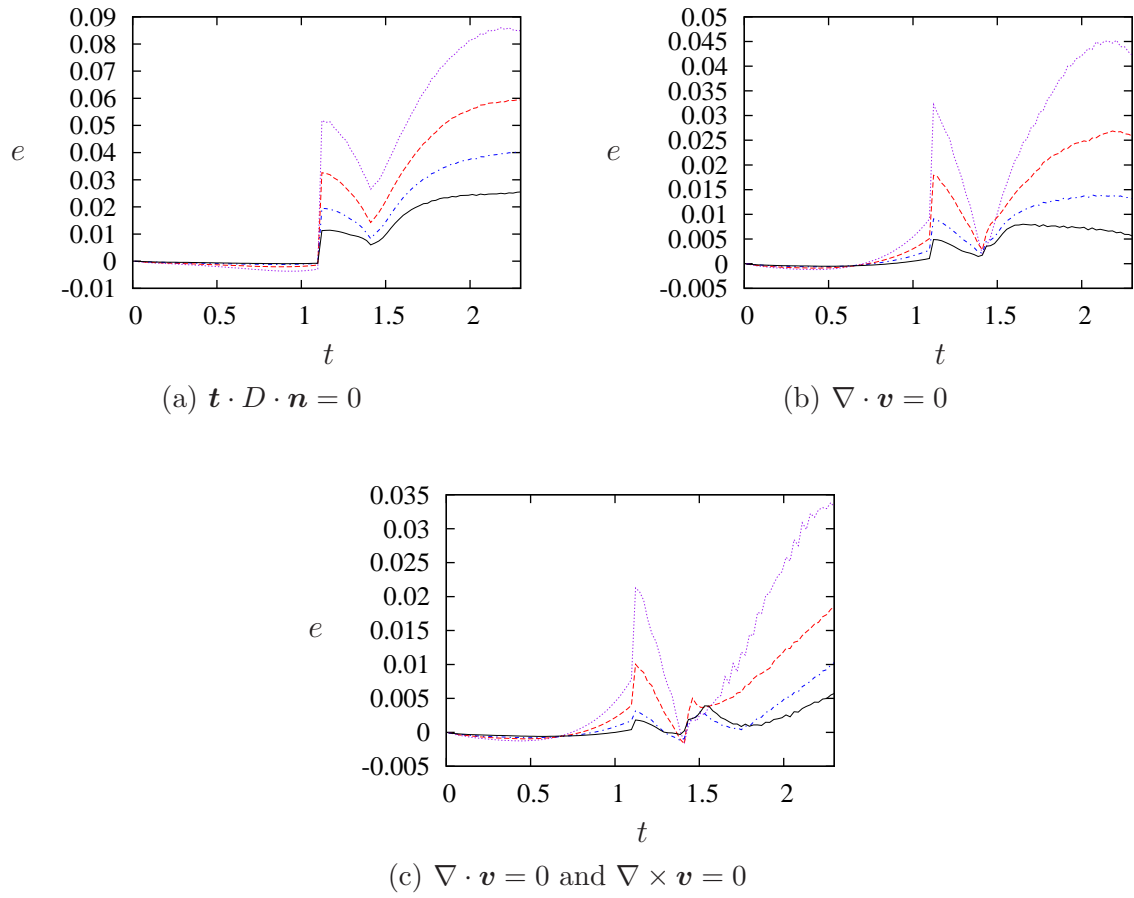
Figure 15: Relative error, $e = [\max(\eta_{BEM}) - \max(\eta_{NS})]/\max(\eta_{BEM})$, for different boundary conditions. Solid line: 512×512 points; dash-dot line: 256×256 points; dashed line: 128×128 points; dotted line: 64×64 points.

3.4 Plunging wave on a beach

The last application that is included in this study is a plunging wave and the results are compared with the BEM-reference solution. A linear beach is assumed in the analysis and the initial condition is a solitary wave on a beach that is calculated from the BEM solver. This setup will cause a large plunger and "Chain of Markers" method will be compared with the reference solution.

The initial condition is the result of a solitary wave with $a/H = 0.5$ at constant water depth and the wave has been propagating towards a linear beach with an inclination of 5.1 deg. The initial condition is calculated from the BEM solver and the initial condition is taken at $t = 13.0$, refer to figure 16. Numerical parameters and mesh properties are listed in table 6.

Convergence tests are executed and results are presented in table 7 and 8, and figure 17 to 20. To calculate the L^2-norm of the error a reference solution (BEM) with $\Delta x = 3.58\text{E-}02$ (grid no. 15) is used. The results show that the error is reduced when increasing the mesh density, as expected. Mass conservation is not perfect with the "Chain of Markers" method and a small loss/gain of mass is observed, refer to table 9.

A comparison for the different boundary conditions at the free surface is compared with the BEM solver in figure 21 to 23. For the boundary condition with zero tangential stress on the free surface, $\boldsymbol{t} \cdot D \cdot \boldsymbol{n} = 0$, large differences are seen between the two different solvers. For the other two cases, incompressible flow, and incompressible and irrotational flow, it is seen a much better agreement between the two solvers. Especially the results in figure 23, where it is assumed both incompressible and irrotational flow, must be considered very good for a Navier-Stokes solver.

Table 6: Numerical parameters for the plunger simulations.

Grid		BC	Δt_{min}	Smoothing (S)	T_{smooth}	N_x	N_y	INP
Grid size	Δx							
256×32	0.051	All	0.0001	200	1.0	5	5	0.5
512×64	0.025	All	0.0001	200	1.0	5	5	0.5
1024×128	0.012	1,2	0.0001	200	1.0	5	5	0.5
1024×128	0.012	3	0.0001	400	1.0	6	6	0.7

Comments:
- Boundary condition (BC). 1: $\boldsymbol{t} \cdot D \cdot \boldsymbol{n} = 0$; 2: $\nabla \cdot \boldsymbol{v} = 0$; 3: $\nabla \cdot \boldsymbol{v} = 0$ and $\nabla \times \boldsymbol{v} = \boldsymbol{0}$.
- Minimum time step, Δt_{min}.
- Smoothing. 5-point smoothing with relaxation is applied and the relaxation parameter α is calculated from $S = \alpha T_{smooth}/\Delta t$.
- N_x, N_y. Refer to section 2.3.3.
- INP. Volume fraction; a cell is included for the extrapolation of velocities if the volume fraction is greater than INP (INP=1: full cell; INP=0: empty cell).
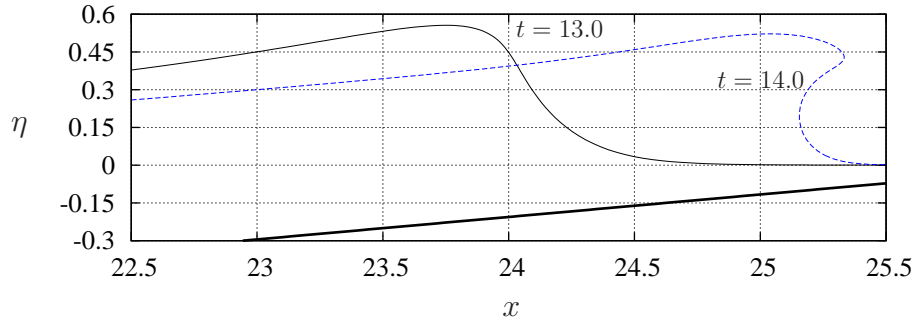
Figure 16: The initial condition of the "Chain of Markers" code is taken at $t = 13.0$ from the BEM-reference solution.

Table 7: Convergence test for the BEM method at $t = 14.6$.

Grid no.	Δx	Norm
5	1.07E-01	1.55E-03
7	7.67E-02	3.29E-04
9	5.96E-02	7.90E-05

Table 8: Convergence test for the "Chain of Markers" method at $t = 14.6$.

		Norm		
BC Grid		$\boldsymbol{t} \cdot D \cdot \boldsymbol{n} = 0$	$\nabla \cdot \boldsymbol{v} = 0$	$\nabla \cdot \boldsymbol{v} = 0,$ $\nabla \times \boldsymbol{v} = \boldsymbol{0}$
Grid size	Δx			
256×32	5.06E-02	-	1.14E-01	6.03E-02
512×64	2.49E-02	1.08E-01	3.80E-02	1.05E-02
1024×128	1.24E-02	6.07E-02	1.41E-02	3.08E-03

Table 9: Mass conservation $\max(|M(t) - M(0)|/M_R)$ for different boundary conditions (BC) and grids, $13.0 \le t \le 14.6$. M_R is a reference mass and equals the mass above $z = 0$ for $t = 0$. A negative value means loss of mass.

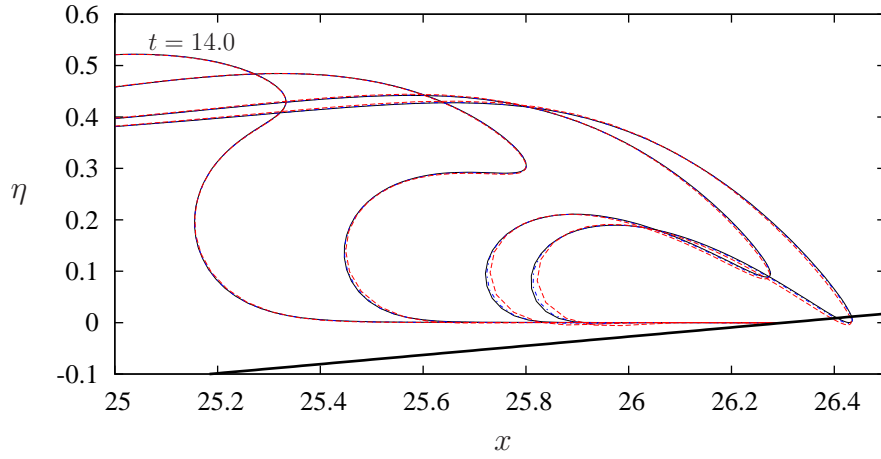|		Mass conservation		
BC Grid		$\boldsymbol{t} \cdot D \cdot \boldsymbol{n} = 0$	$\nabla \cdot \boldsymbol{v} = 0$	$\nabla \cdot \boldsymbol{v} = 0,$ $\nabla \times \boldsymbol{v} = \boldsymbol{0}$
Grid size	Δx			
256×32	5.06E-02	1.04E-03	-3.68E-03	-6.55E-03
512×64	2.49E-02	5.15E-04	-1.66E-04	-1.61E-03
1024×128	1.24E-02	5.89E-04	5.40E-04	-4.55E-03

Figure 17: Convergence test for the reference solution BEM, $t = \{14.0, 14.3, 14.6, 14.7\}$. Solid line: n9; dash-dot line: n7; dashed line: n5.
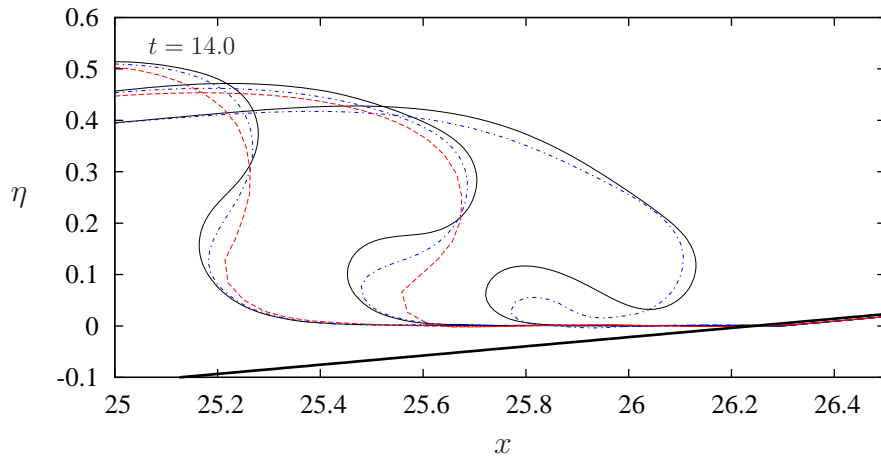

Figure 18: Convergence test when $\boldsymbol{t} \cdot D \cdot \boldsymbol{n} = 0$, $t = \{14.0, 14.3, 14.6\}$. Solid line: 1024×128; dash-dot line: 512×64; dashed line: 256×32.
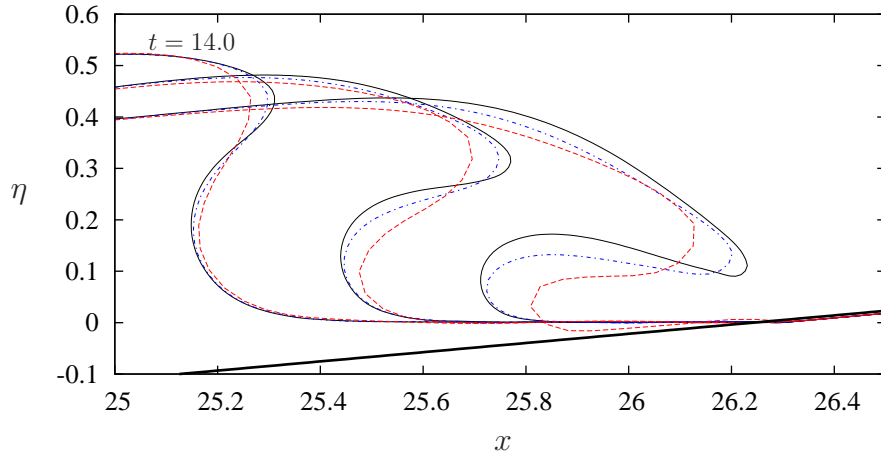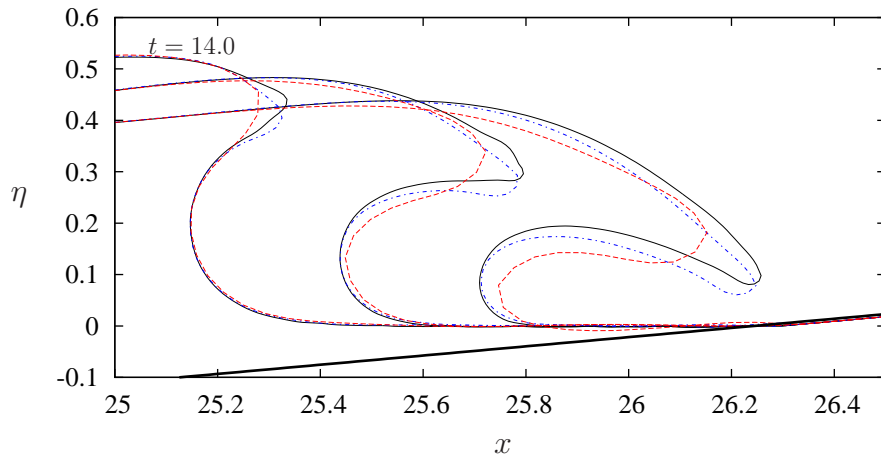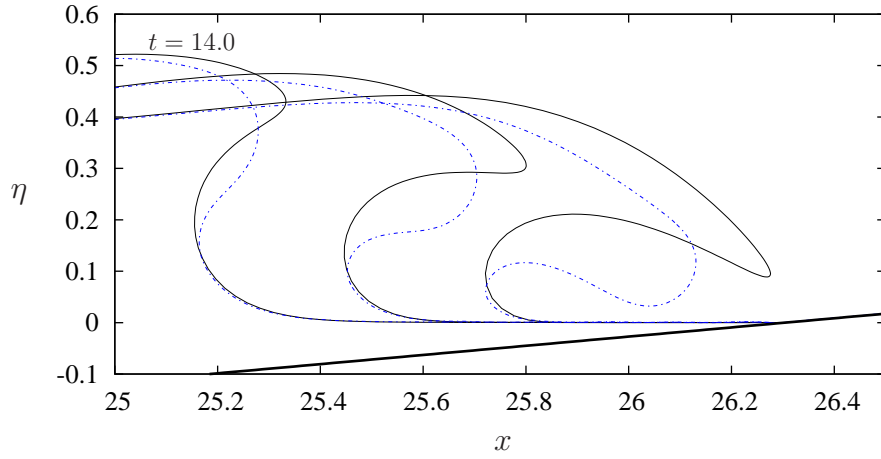
Figure 19: Convergence test when $\nabla \cdot \boldsymbol{v} = 0$, $t = \{14.0, 14.3, 14.6\}$. Solid line: 1024×128; dash-dot line: 512×64; dashed line: 256×32.

Figure 20: Convergence test when $\nabla \cdot \boldsymbol{v} = 0$ and $\nabla \times \boldsymbol{v} = 0$, $t = \{14.0, 14.3, 14.6\}$. Solid line: 1024×128; dash-dot line: 512×64; dashed line: 256×32.

Figure 21: Comparison for the times $t = 14.0, 14.3, 14.6$. Surface constraint: Zero tangential stress on the free surface. Solid line: BEM; Dash-dot: "Chain of Markers".
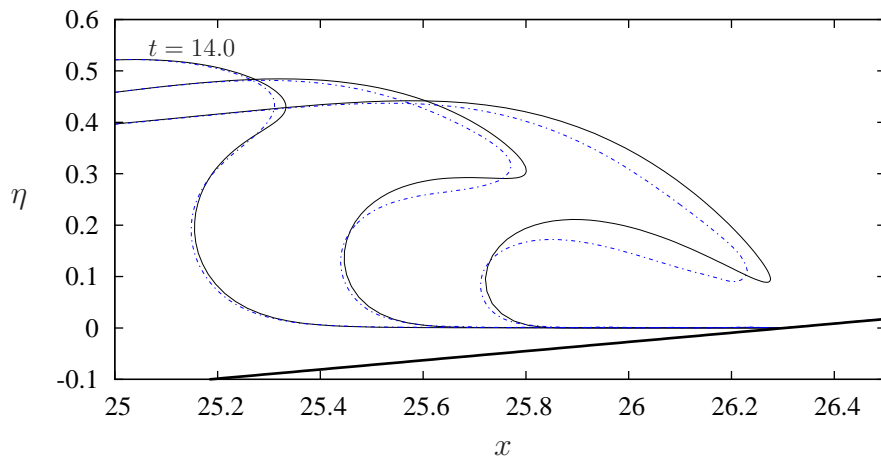

Figure 22: Comparison for the times $t = 14.0, 14.3, 14.6$. Surface constraint: Incompressible fluid. Solid line: BEM; Dash-dot: "Chain of Markers".
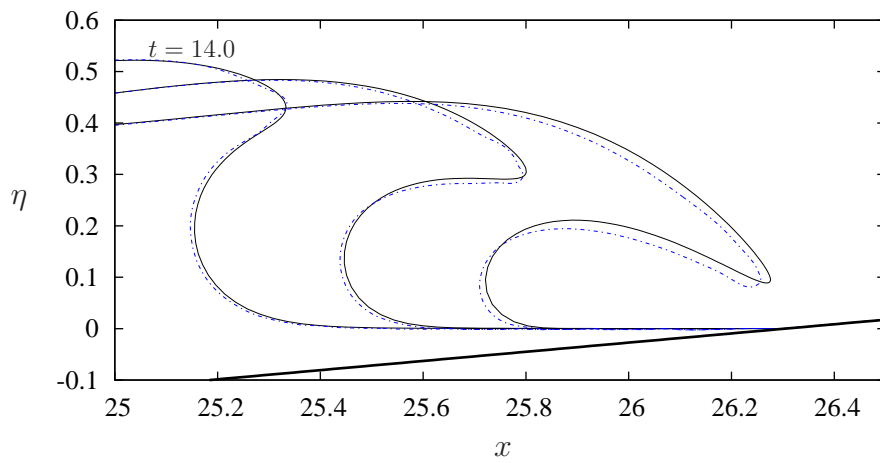
28

Figure 23: Comparison for the times $t = 14.0, 14.3, 14.6$. Surface constraint: Incompressible and irrotational fluid. Solid line: BEM; Dash-dot: "Chain of Markers".

4   Conclusions

A comparison between the "Chain of Markers" code and a BEM solver has been presented. Special attention is paid to the treatment of the free surface and its boundary conditions. From the examples presented it is concluded that incorporating the boundary condition of surface tension requires a very fine grid when the Reynolds number is large. For large Reynolds number better results are achieved when neglecting the surface tension and only imposing a constraint of an incompressible fluid. When comparing the results to a BEM solver the best agreement was obtained with two constraints imposed at the free surface; incompressible fluid and irrotational flow. This is expected since the boundary element method is based on incompressible and irrotational flow.

If the "Chain of Markers"code shall give good results for large scale problems where surface tension is included, this will require a very fine mesh in the vicinity of the free surface. One possibility is to re-write the "Chain of Markers"code to have a dynamic grid that is locally refined in the vicinity of the free surface. However, the mesh in the "Chain of Markers"-code is a static and regular grid ($m \times n$ cells) and re-writing the code to be able to handle a dynamic grid with local refinement will be a very comprehensive extension.

5   Acknowledgment

References

[1] A. Brandt. *Guide to multigrid development.* Springer, 1982. 6

[2] W. L. Briggs. *A multigrid tutorial.* SIAM, Philadelphia, 1987. 6

[3] P. M. Gresho and R. L. Sani. *Incompressible flow and the finite element method.* Wiley, 1998. 5

[4] E. V. Laitone. The second approximation to cnoidal and solitary waves. *J. Fluid Mech.*, 9:430–444, 1960. 11

[5] H. Lamb. *Hydrodynamics.* Cambridge University Press, sixth edition, 1932. 9

[6] H. P. Langtangen, K.-A. Mardal, and R. Winter. Numerical methods for incompressible viscous flow. *Advances in Water Resources*, 25(8-12):1125–1146, August-December 2002. 5

[7] M. S. Longuet-Higgins and J. D. Fenton. On the mass, momentum, energy and circulation of a solitary wave. II. *Proc. Roy. Soc. London. A*, 340:471–493, 1974. 11

[8] G. Pedersen. Variable depth and the validity of Boussinesq-type models. *PREPRINT SERIES, Mechanics and Applied Mathematics* (ISSN 0809-4403), 2005. http://urn.nb.no/URN:NBN:no-27784. 11, 15

[9] S. Popinet and S. Zaleski. Bubble collapse near a solid boundary: a numerical study of the influence of viscosity. *J. Fluid Mech.*, 464:137–163, 2002. 1, 2, 3, 6

[10] J. Wesseling. *An introduction to multigrid methods*. Wiley, 1992. 6

[11] G. B. Whitham. *Linear and nonlinear waves*. Pure and Applied Mathematics. Wiley-Interscience, 1974. 11

[12] J. Witting. On the highest and other solitary waves. *SIAM J. Appl. Math.*, 28(3):700–719, 1975. 11